Exp Fluids (2016) 57:178
DOI 10.1007/s00348-016-2268-8

RESEARCH ARTICLE

Void waves propagating in the bubbly two-phase turbulent boundary layer beneath a flat-bottom model ship during drag reduction

Hyun Jin Park[1] · Yoshihiko Oishi[2] · Yuji Tasaka[1] · Yuichi Murai[1]

Received: 1 August 2016 / Revised: 12 October 2016 / Accepted: 21 October 2016

Abstract The injection of bubbles into a turbulent boundary layer can reduce the skin friction of a wall. Conventionally, the drag reduction rate is evaluated using time-averaged quantities of the mean gas flow rate or mean void fraction. Actually, as bubbles are subject to strong shear stresses near the wall, void waves and local bubble clusters appear. For pipe and channel flows, such wave-like behavior of the dispersed phase has been investigated intensely as an internal two-phase flow problem. We investigate how this wavy structure forms within the boundary layer as an external spatially developing two-phase flow along a horizontal flat plate. We describe how our model ship is designed to meet that purpose and report bubble-traveling behavior that accompanies unexpectedly strong wavy oscillations in the streamwise direction. A theoretical explanation based on a simplified two-fluid model is given to support this experimental fact, which suggests that void waves naturally stand out when drag reduction is enhanced through the local spatial gradient of the void fraction.

List of symbols

C	Void wave propagation speed (m/s)
Ca	Cavitation number (dimensionless)
C_f	Frictional coefficient (dimensionless)
d_{cb}	Distance between the closest pair of bubbles (m)
d_e	Equivalent diameter of bubble (m)
Fr	Froude number (dimensionless)
f	Local instantaneous volume fraction of liquid phase (dimensionless)
f_G	Local instantaneous void fraction (dimensionless)
f_{void}	Frequency of voidage wave (Hz)
G_1	Impact factor of drag reduction to void fraction in the boundary layer (dimensionless)
G_2	Impact factor of drag reduction to local gradient of void fraction (m)
g	Acceleration due to gravity (m/s^2)
H	Height of the model ship (m)
h	Thickness of the reflective index matching material (m)
L	Length of the model ship (m)
l_τ	Friction length (m)
p	Local pressure of the water (Pa)
p_v	Vapor pressure of the water (Pa)
Q_g	Injected gas flow rate (m^3/s)
Q_l	Liquid flow rate in the boundary layer (m^3/s)
Re_x	Reynolds number on a flat plate (dimensionless)
t	Time (s)
t_g	Apparent air layer thickness (m)
U_{main}	Main flow velocity (equivalent to towing speed) (m/s)
U_δ	Averaged flow velocity in the boundary layer (m/s)
u, v, w	Velocity components in x, y, z directions (m/s)
u_b	Averaged advection velocity of bubbles (m/s)
u_y	Averaged streamwise velocity at each depth (m/s)
V	Averaged downward velocity of liquid phase on the border of the boundary layer (m/s)
W	Width of the model ship (m)
x, y, z	Cartesian coordinates of the model ship (m)

✉ Hyun Jin Park
park@eng.hokudai.ac.jp

[1] Laboratory for Flow Control, Division of Energy and Environmental Systems, Faculty of Engineering, Hokkaido University, N13 W8, Kita-ku, Sapporo 060-8628, Japan

[2] Fluid Engineering Laboratory, College of Design and Manufacturing Technology, Muroran Institute of Technology, 27-1, Mizumoto-cho, Muroran 050-8585, Japan

Published online: 19 November 2016

α_δ	Void fraction in the boundary layer (dimensionless)
δ	99% thickness of the boundary layer (m)
δ_g	Superficial air layer thickness (m)
μ	Viscosity of water (kg/m s)
ν	Kinematic viscosity of water (m^2/s)
ρ	Density of water (kg/m^3)
τ_w	Wall shear stress (Pa)
τ_{w0}	Wall shear stress in single-phase flow (Pa)

1 Introduction

Bubbly drag reduction (BDR) is a collective term for attempts to reduce drag by injecting bubbles into turbulent boundary layers. Over the past four decades, it has received attention as a means to decrease fuel consumption of large marine vessels. Several successes of BDR in sea trials have been recently reported in the literature (Mizokami et al. 2013; Jang et al. 2014; Kumagai et al. 2015). These groups have confirmed independently good reproducibility in fuel-saving performance ranging from 5 to 15% for different types of vessels. In academic fields, drag reduction performance and its parametric dependency have been investigated experimentally with in-house flow geometries such as a horizontal channel flows. We have found hundreds of papers on BDR since its first reporting by McCormick and Bhattacharyya (1973). In idealized conditions, local drag reduction rates of 80% can be achieved (e.g., Madavan et al. 1984). Nevertheless, there is a gap between ideal and practical conditions; the recent success for ships relies on expertise obtained with fundamental two-phase flow experiments. For further improvements in drag reduction performance, the behavior of bubbles skimming along a ship's hull during BDR operations needs clarification. There are two reasons for this requirement. One is the difficulty in extrapolative expectations on how bubbles travel beneath a hull of a real ship from simply laboratory-downsized results. Reynolds number are of much higher order in real ships than those in-house, whereas Froude number can be set by reducing the length scale. The other is that the dominant BDR mechanism changes undesirably depending on a combination of dimensionless numbers associated with bubbles, such as Weber number in turbulence. In the review article on BDR performance by Ceccio (2010), disparate results in different facilities were reported despite a similar volume fraction of bubbles treated. Murai (2014) stressed the complexity of parametric combinations in two-phase turbulence while classifying the drag reduction mechanism over a two-dimensional parameter space given by bubble size and main flow velocity.

BDR uses dispersed bubbles in the turbulent boundary layer, and therefore bubbles are distributed more or less non-uniformly along the wall. Even with a random distribution, bubbles inevitably exhibit local non-uniformity. In addition to the randomness, the Lagrangian motions of individual bubbles accompanying the slip velocity in the liquid phase will amplify this non-uniformity. For vertical pipe geometry, there are several reports dealing with bubble non-uniformity that enhances the flow transition (Lisseter and Fowler 1992; Lammers and Biesheuvel 1996). Bubble clusters can be generated as the slip velocity brings bubbles closer together. This clustering was clearly observed in free-rising bubble flow by Kitagawa et al. (2004) and Mercado et al. (2010), in vertical bubbly channel flow by Takagi and Matsumoto (2011), and also in horizontal bubbly channel flow by our group (Murai 2014).

Viewed in the Eulerian frame, these are identified as void fluctuations in time and space. Here two questions arise when considering the relationship between void fluctuation and drag reduction performance. One is how such fluctuations are amplified in the main direction of flow as it interacts with the turbulent boundary layer. The other is how fluctuations affect the average drag reduction rate. Oishi et al. (2009) found in their channel flow experiments that a local void fluctuation, which was generated naturally within a boundary layer, contributes positively to a time-averaged drag reduction. They also detected a significant phase delay in the local void fraction with respect to the local drag reduction. Pursuing the mechanism hidden in this fact, Park et al. (2015a) generated artificial void waves by repetitive bubble injections at the upstream location of a fully developed horizontal channel flow. They confirmed that BDR performance was improved significantly by generating these artificial void waves.

The above-mentioned in-house experiments also alert marine vessel designers that they need to be careful of void waves, which may occur around ship hulls. There has been no attempt yet to quantitatively visualize the void fluctuation in an actual application of BDR to ships. The vast difference between model ships of in-house experiments and marine vessels may be whether the system is closed or opened in terms of the two-phase turbulent boundary layer. While channel flow experiments inquire bubble–turbulence interaction in fully developed turbulence between two parallel walls, marine vessels apply bubbles in spatially developing boundary layers open to outer potential flows. The main question we try to solve experimentally is whether void waves emerge stronger in an open system than in bounded shear flows. To this end, we have designed a fully transparent model vessel, which is essentially equivalent to an experimental cabin cruising in water that allows various bubble behaviors to be quantified visually. In the following, we describe the design features of the model ship to meet this purpose. We then report on the drag reduction performance and its relation to measured statistics of the bubble

Table 1 Details of model ships reported in previous research studying bubbly drag reduction

Researchers and reporting year	Label in Fig. 5	Ship length (m)	Ship speed (m/s)
Titov (1975)	1	8.46	1.0–1.8
Tokunaga (1987)	2	3.5	5–9
Yim and Kim (1996)	3	2.6	1.1–1.3
Watanabe et al. (1998)	4	20	5.0–7.0
	5	40	5.0–7.0
Fukuda et al. (2000)	6	7.267	0.7–1.9
	7	12.0	1–6
Hirayama et al. (2003)	8	16	1.0–7.0
Latorre et al. (2003)	9	2.31	5.7–10.4
Takahashi et al. (2003)	10	12	5–7
	11	50	5–7
Katsui et al. (2003)	12	7	1.0–1.4
Foeth et al. (2010)	13	11.8	3.1–4.9
Amromin et al. (2011)	14	4.55	12.3–16.5
Mäkiharju et al. (2013)	15	12.9	5–7.5
	16	0.912	1.3–2.5
Jang et al. (2014)	17	8.3	6.7–8.2

behavior. Finally, void waves, which stand out strongly in the present flow geometry, are analyzed precisely, supported also by a theoretical discussion based on the simplified two-fluid model equations.

2 Design of experimental model ship

In the study of BDR performance, details of several model ships have already been reported (see Table 1). All these model ships were designed with a flat bottom to avoid bubbles escaping from the target wall. Each model ship successfully obtained a certain level of drag reduction, which depended on a combination of various parameters in operation. Whereas total or pointwise drag reduction was confirmed in these systems, bubble behavior was not carefully measured. We therefore designed a model ship consisting of a transparent flat acrylic plate for visualizing bubbles traveling in the spatially developing boundary layer. Experiments with the model ship were performed in a towing tank to establish conditions of no hydrostatic pressure gradient in the horizontal plane, i.e., the bottom plane of the ship was adjusted horizontally and towed at a constant advancing speed in the stationary water of a large underground pool, 100 m in total length. Details of the model ship and the towing system are explained in Sects. 2.1 and 2.2.

2.1 Model ship incorporating measuring devices

To analyze the formation of void waves at various length scales, the behavior of bubbles and their relevance to drag reduction performance were investigated simultaneously. We designed a model ship that allows various measuring devices to be attached including ultrasonic bubble measurement systems, wall shear stress sensors, and optical bubble-imaging systems. Figure 1 presents schematic diagrams of the model ship; Table 2 lists its dimensions and basic specifications. Except for aluminum rims, the model ship is for the most part made of transparent acrylic resin; its overall length (L) is 4000 mm, width (W) 600 mm, and height (H) 500 mm. The x, y, and z coordinates are defined respectively as the streamwise distance from the leading edge, the vertical downward position from the bottom plate, and the spanwise position from the central axis of the ship. To avoid influences of bow-generated splashing waves to the boundary layer structure, two guide walls protruding 20 mm below the bottom plate are attached to both edges (Fig. 1c). To impose an ideal spatially developing boundary layer on the flat bottom plate, the hull of the ship is completely flat with no ridges and has a smooth plate surface. The leading edge of the bottom plate has a 45° bevel to minimize downstream influences of the front-edge flow separation. For this model ship, we also calculated its center of gravity, meta-center in the body-neutral floating state, and recovery moment vector from various inclined attitudes after the adopted strength of materials were determined in high-speed towing conditions. We omit the description of these design features to focus on the two-phase fluid dynamics of the ship.

The air injector supplying the bubbles consists of a compressor, an airflow rate control system, a buffer chamber of total volume 5.0×10^{-3} m^3, and a multi-hole bubble injection plate having 42 open holes, each of 5 mm diameter

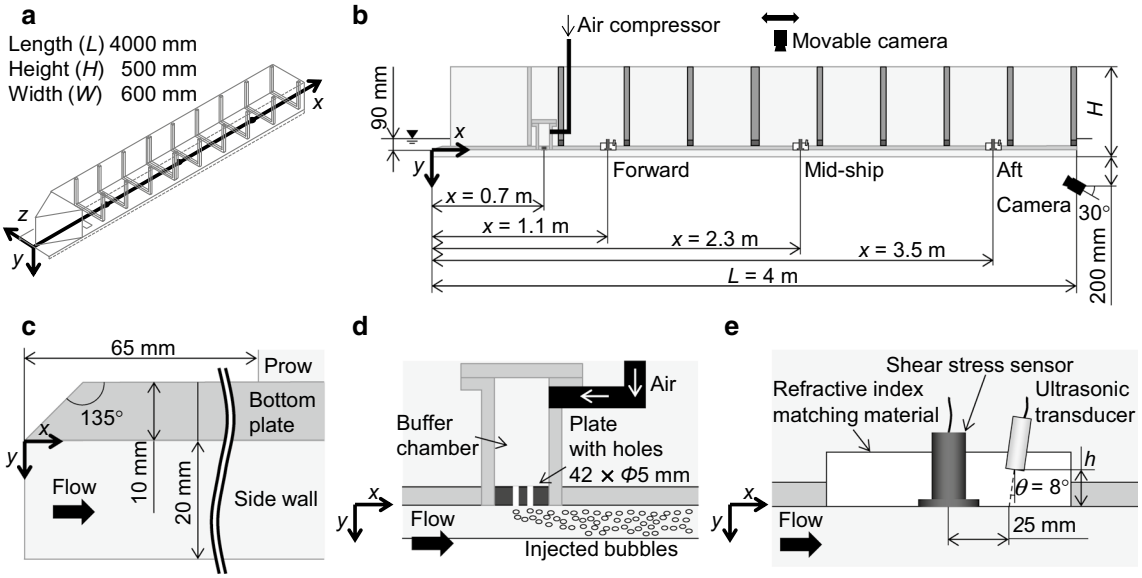

Fig. 1 Schematic diagram of the experimental facility; **a** *top view* of the model ship, **b** *side view* of the model ship, **c** details of the leading edge, **d** schematic of the air injector and **e** combined mounted system of the shear stress and ultrasonic transducers embedded on the bottom plate

Table 2 Dimensions and weight of the model ship

Material	Transparent acrylic resin
Length (*L*)	4000 mm
Height (*H*)	500 mm
Width (*W*)	600 mm
Weight (unloaded)	149 kg
Draft (unloaded)	68 mm

(see Fig. 1d). The bubble injection plate is located 0.7 m downstream from the leading edge. A servo valve in the airflow rate control system is operated and managed automatically by a PC to supply air with a constant stable volume flow rate (see Fig. 2). The control system for the airflow rate is designed similar to a device developed by Tokyo Gas Corporation (Takeuchi and Kagawa 2013) which is able to supply air at constant volume flow rate up to 2.5×10^{-3} m^3/s. Pressure logs in the buffer chamber for air injection are shown in Fig. 3, where the unit is in gauge pressure, i.e., pressure differential increase from atmospheric pressure. In our system, the flow rate of air supply is kept mostly constant in time and standard deviation of the temporal fluctuation relative to mean value was smaller than 1%. The power spectra of the corresponding condition are shown at right panels. The spectra do not include strong peaks (note that the scale of the ordinate is three digits different from the left panels) and can be regarded as white-noise pattern. From this, it can be denied that the void waves observed downstream come straightforward from the initial fluctuation in air injection flow rates.

To record bubble motion, two cameras were installed on the model ship (Fig. 1b). One was a high-speed video camera (FASTCAM Mini UX 100, Photron, Ltd.) set above the hull. The camera was mounted on two parallel rails that enabled the photographing location to change in the main

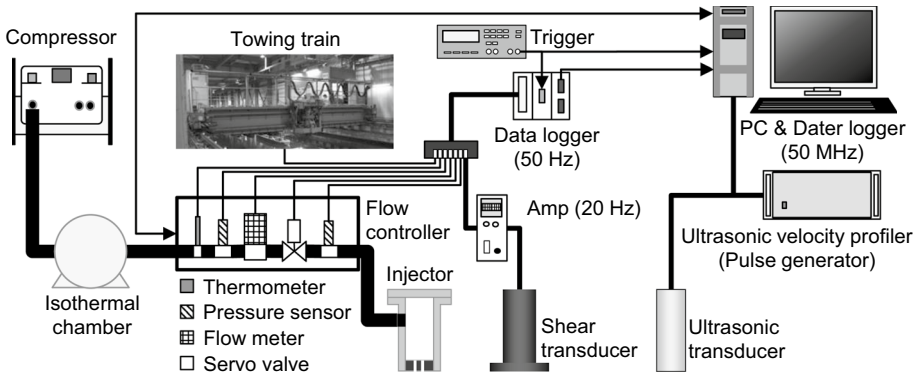

Fig. 2 Schematic diagram of the flow control system synchronized and integrated with multiple measuring devices

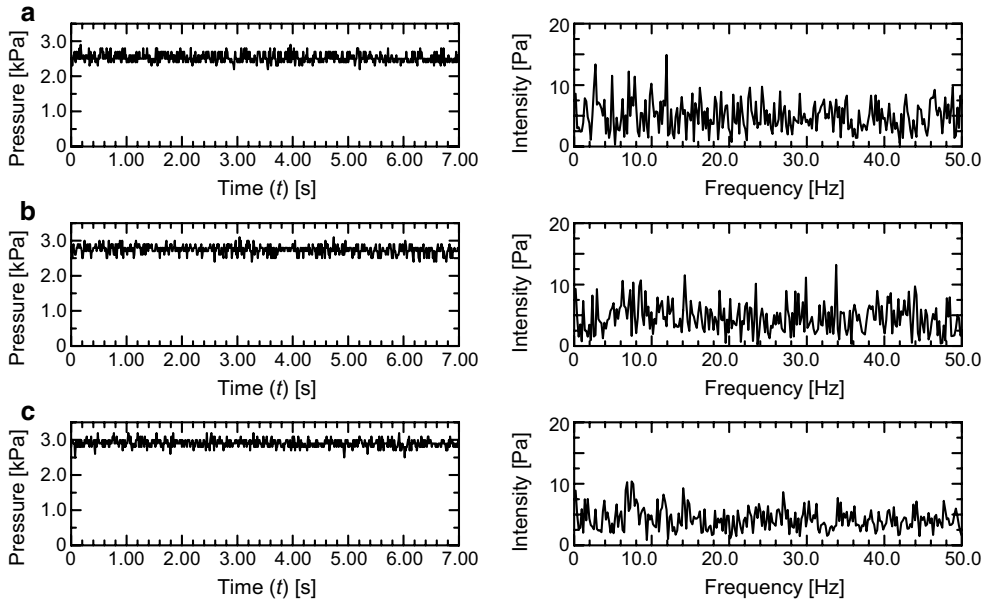

Fig. 3 Time series of pressure in buffer chamber (*left side*) and linear spectra (*right side*) at $Q_g = 1.67 \times 10^{-3}$ m^3/s; **a** $U_{main} = 2.00$ m/s, **b** 2.50 m/s and **c** 3.00 m/s

direction of flow. The camera recorded a local top view image of the bubbles through the transparent bottom of the ship, from which size, shape, and velocity of individual bubbles were obtained. The other was a waterproof camera (HERO3, GoPro, Inc.) set near the rear edge of the ship bottom plate under the water line. This camera recorded all of the bubbles flowing beneath the bottom plate from an oblique direction. In imaging the bubble, three light sources were used and arranged after several trial-and-error attempts to optimize the field of illumination. Basically, the top viewing of bubbles relies on underwater lighting of six large white screens laid on the bottom of the water reservoir. Each screen is 3 m in length and 8 m in width and is placed at 4-m intervals. Because the white screens reflect diffuse light upward, the images captured the bubbles as backlit shadows. However, this is insufficient for identifying film-state bubbles, and we implemented underwater lateral lighting as well. Furthermore, a metal halide lamp supplemented lighting inside the model ship to detect bubbles smaller than 0.5 mm. The camera then captured strong light-scattering points of all spherical bubbles.

A combined system of shear stress sensor (S10W-4, SSK Co., Ltd, Tokyo, Japan.) and ultrasonic transducer was installed at three points along the direction of flow, 1.1, 2.3 and 3.5 m from the leading edge; these are hereafter referred to as forward, mid-ship, and aft, respectively. The same type of shear transducer was used in previous studies to monitor the local wall shear stress in bubbly two-phase flows (Kodama et al. 2000; Takahashi et al. 2003; Park et al. 2015a). The frequency response characteristics of the shear transducer were reported by Murai et al. (2007); the temporal resolution is about 20 Hz. Signals from the shear transducers, airflow rate control system, and the velocity of the towing train are recorded simultaneously into a data logger (NR-500, KEYENCE Co.) as shown in Fig. 2. This signal integration allows us to monitor the drag reduction performance in real time during the ship-towing operation. To determine the vertical interfacial position of bubbles away from the bottom plane, ultrasonic bubble echography developed within our group was applied, details of which were reported by Park et al. (2015b). The ultrasonic transducer was embedded inside the bottom wall at a tilt angle of $\theta = 8°$ to the vertical direction. The transducer is located at approximately 28 mm away from the shear transducer, both of which are collocated in a disk-hold combined mount system (Fig. 1e). Furthermore, an ultrasonic velocity profiler (UVP-DUO MX, MET-FLOW S.A., Lausanne, Switzerland) was adopted not only for use in velocity profile measurements of the liquid phase but also as the ultrasonic pulse generator in the bubble echography. Table 3 summarizes the parameter settings for all instrumentation.

In this paper, we report on drag reduction performance of the present model ship and focus in particular on the bubble behavior that is observed using the two bubble-imaging techniques recorded by the top-viewing high-speed camera and the underwater camera. Liquid velocity and bubble echography information will be reported separately.

Table 3 Parameters of the measuring instruments

Shear stress sensor	
Measurement area	25π mm^2
Temporal resolution	20 Hz
Range of shear stress	±250 Pa
Ultrasonic pulse generator and ultrasonic transducer	
Ultrasonic basic frequency	4 MHz
Number of cycle	4
Pulse repetition frequency	3.2 kHz
Voltage for ultrasonic emission	150 V
Ultrasonic beam diameter	5 mm
Divergence half-angle	2.2°
Data logger for echography	
Sampling frequency	50 MHz
Range of voltage	±2 V
Resolution of voltage	4 mV
Camera above the ship	
Frame rate	500 fps
Resolution	0.08 mm/pixel
Underwater camera	
Frame rate	120 fps

2.2 Towing test facility

The present series of experiments was performed at a large towing test facility in Hiroshima University, Japan. The facility is certified as a standards institute for ship performance examination, which was registered by ISO 9001 (International Standard Organization) in 2012. The towing test facility comprises a 100-m-long rectangular water reservoir and a powerful towing train (Fig. 4a, b).

The train is a large steel carriage that runs on two parallel rails either side of reservoir and running along its full length. The motion of the train is managed by the operator at the cockpit above the train. Speeds of the train are controlled. Table 4 summarizes dimensions, performance, and conditions of the present towing test facility. Two rigid pillars inside the train support our model ship (Fig. 4c). The support system does not allow the model ship to incline because of hydrodynamic moments, i.e., pitching, yawing, and rolling do not occur in towing operations. The bottom plane of the ship was fixed horizontally at 90 mm below the water surface. This depth is close to the natural draft of the ship determined by the balance between weight and buoyancy. To mitigate hydrostatic pressure gradient along at the bottom plane, we adjusted the water depth precisely to be the same along the entire ship bottom. Because of safety issue associated with limits in train deceleration, the model ship travels approximately 80 m. Within this distance, train acceleration and deceleration further reduce the available distance in constant-speed testing. Under the maximum possible speed, the duration for steady-state operation is 7 s or 21 m in distance.

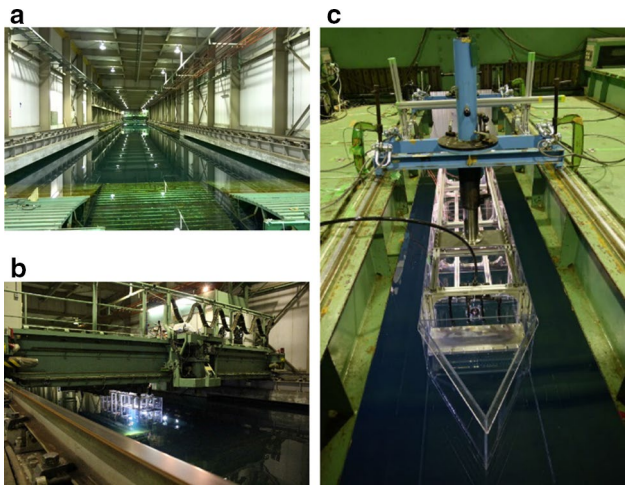

Fig. 4 Photographs of the ship-towing test facility in Hiroshima University; **a** towing water reservoir, **b** towing train and **c** model ship hooked up to the train

2.3 Experimental conditions

The two controllable parameters of the present experiment are towing speed (U_{main}) and air volume flow rate (Q_{g}). U_{main} ranges from 2.00 to 3.00 m/s, at which the superficial air layer thickness (δ_{g}) defined by

$$\delta_{\mathrm{g}} = \frac{Q_{\mathrm{g}}}{U_{\mathrm{main}} W}. \tag{1}$$

is maintained below 2 mm; here W denotes the spanwise width of the ship, which is 600 mm in the present model ship. This air layer thickness is often used in experimental studies for BDR because it roughly estimates the displacement thickness of the liquid velocity boundary layer agitated by bubbles. Figure 5 shows a comparison of present experimental conditions with those of past studies (see Table 1) mapped on the parameter space of U_{main} and L. On the map, the oblique lines indicate the contours of Froude number defined as

$$Fr = \frac{U_{\mathrm{main}}}{\sqrt{gL}}. \tag{2}$$

The horizontal line in the map indicates the unit contour of the cavitation number defined by

$$Ca = \frac{2(p - p_{\mathrm{v}})}{\rho U_{\mathrm{main}}^2}. \tag{3}$$

Here, g, p and p_{v} are the acceleration due to gravity, the local static pressure at the ship bottom, and the vapor

Table 4 Dimensions, performance and conditions of the towing test facility

Water reservoir	
Length in towing direction	100 m
Depth	3.5 m
Width	8.0 m
Content in the tank	Water (clean city water)
Temperature of water	29 °C
Density of water (ρ)	996 kg/m^3
Kinematic viscosity of water (ν)	0.847×10^{-6} m^2/s
Surface tension of water	71.2×10^{-3} N/m
Speed of sound in water	1507 m/s
Towing train	
Length	8 m
Weight	20×10^3 kg
Total power of the towing train by four electric cells	65 kW
Maximum speed	3.00 m/s
Minimum speed	0.10 m/s
Variable range of acceleration	0.1–0.8 m/s^2
Period of constant towing speed at maximum speed	7.0 s

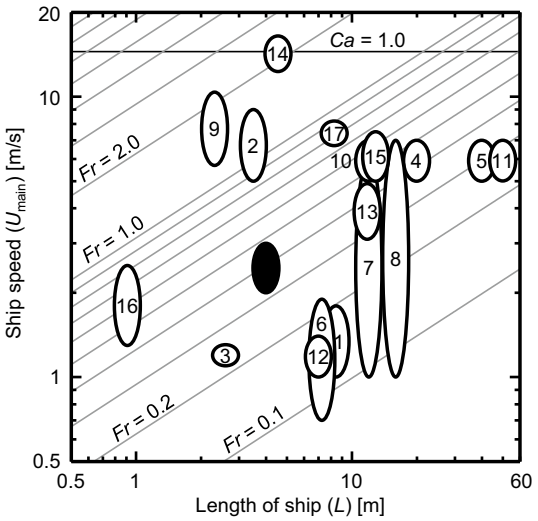

Fig. 5 Ellipse plots of the experimental parameter conditions examined in the past relative to the present experimental condition (*closed ellipse*); *numbers labeling open ellipses* correspond to the experimental ships listed in Table 1

pressure of the water, respectively. For reference, a line is drawn assuming a water depth of 100 mm. In actual situations, large vessels such as container carriers and oil tankers sail at $Fr \leq 0.3$ so as not to intensify their wave making resistance. Although Fr in our experiments is larger than 0.3, the wave does not affect the BDR phenomena at the bottom plane because the model ship is fixed in altitude,

Table 5 Experimental conditions of bubble injection into spatially developing boundary layer

Controlled parameters	
Towing speed	2.00–3.00 m/s
Air volume flow rate (Q_g)	0.42×10^{-3}–2.50×10^{-3} m^3/s
At the bubble injector, x = 0.7 m	
Reynolds number (Re_x)	1.6×10^6–2.5×10^6
Thickness of the boundary layer (δ)	13.6–14.8 mm
Void fraction inside the boundary layer (α_δ)	1.9–16.1%
At the forward, x = 1.1 m	
Reynolds number (Re_x)	2.6×10^6–3.9×10^6
Thickness of the boundary layer (δ)	19.6–21.2 mm
Void fraction inside the boundary layer (α_δ)	1.4–11.2%
At the mid-ship, x = 2.3 m	
Reynolds number (Re_x)	5.4×10^6–8.1×10^6
Thickness of the boundary layer (δ)	35.3–38.3 mm
Void fraction inside the boundary layer (α_δ)	0.7–6.2%
At the aft, x = 3.5 m	
Reynolds number (Re_x)	8.2×10^6–1.2×10^7
Thickness of the boundary layer (δ)	49.4–53.6 mm
Void fraction inside the boundary layer (α_δ)	0.5–4.4%

and also the side walls separate the BDR-target bottom plane from the outer flow.

On the target plane, the Reynolds number defined by

$$Re_x = \frac{xU_{\text{main}}}{\nu}, \tag{4}$$

where x and ν are the streamwise distance from the front edge of the bottom plate and kinematic viscosity of water, respectively, describes the dynamic similarity of the spatially developing boundary layer for single-phase flow. Generally, a turbulent boundary layer forms on a flat plate at $Re_x > 5 \times 10^5$. Thus, for the present model ship, a turbulent state is reached 0.25 m from the front edge, which is forward of the point of bubble injection at 0.70 m from the front edge.

The air volume flow rate (Q_g) is regulated at fixed values taken from the range 0.42×10^{-3} to 2.50×10^{-3} m^3/s. The void fraction inside the turbulent boundary layer is estimated by

$$\alpha_\delta = \frac{Q_g}{Q_l + Q_g} \approx \frac{Q_g}{W \int_0^\delta u_y \mathrm{d}y} \approx \frac{Q_g}{W \int_0^\delta U_{\text{main}} \left(\frac{y}{\delta}\right)^{\frac{1}{7}} \mathrm{d}y}, \tag{5}$$

where we assume the initial liquid phase velocity distribution (u_y) is given to estimate the liquid volume flow rate inside the turbulent boundary layer. In single-phase flow,

the boundary layer thickness (δ) spatially increases downstream as estimated by

$$\delta = 0.37x^{\frac{4}{5}}\left(\frac{\nu}{U_{\mathrm{main}}}\right)^{\frac{1}{5}}. \tag{6}$$

Equations (5) and (6) imply that the mean void fraction inside the boundary layer, α_δ, decreases downstream when U_{main} and Q_{g} are fixed. However, when drag reduction occurs, the local instantaneous values of Q_{g} and u_y couple in the space–time domain along the wall. This aspect is our focus of attention in the rest of the paper. All other details of the experimental conditions are listed in Table 5.

3 Performance of the model ship

In this section, we present the basic drag reduction performance obtained with the present model ship and the detailed conditions of bubbles streaming beneath the bottom plane.

3.1 Wall shear stress

Figure 6a shows the relationship between the wall shear stress with no bubble injection (τ_{w0}) measured at the three locations and several U_{main}. Wall shear stress increases with ship speed more than linearly but less than quadratic. This trend agrees in general with a previous study using a towing flat plate (e.g., Mori et al. 2009). Of the three locations, the forward location has a wall shear stress higher than the other two aft locations. This is explained by the expanding thickness of the boundary layer along the main direction of flow. Figure 6b shows the same trend plotted in the two-dimensionless parameter space, i.e., Re_x and coefficient of friction which is defined by

$$C_{\mathrm{f}} = \frac{2\tau_{\mathrm{w0}}}{\rho U_{\mathrm{main}}^2}. \tag{7}$$

The two curves refer to the Blasius friction law for laminar boundary layer flows and the empirical coefficient of friction for the turbulent state by Schlichting (1979). The corresponding formulae are given by

$$C_{\mathrm{f}} = 1.328Re_x^{-1/2} \tag{8}$$

for laminar flow, and

$$C_{\mathrm{f}}e^{-0.558C_{\mathrm{f}}^{-1/2}} = Re_x^{-1} \tag{9}$$

for turbulent flow. The measured data points support the notion that the present flat bottom ship properly forms a spatially developing turbulent boundary layer in accordance with Schlichting's formula.

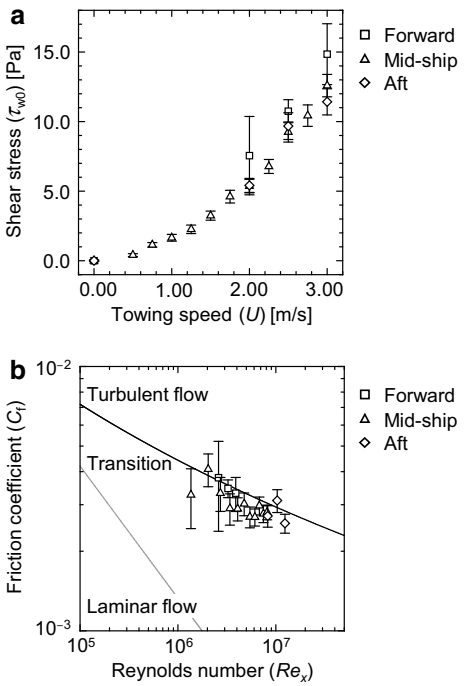

Fig. 6 Frictional drag of the model ship in single-phase flow conditions, where *error bars* indicate standard deviations of the temporal fluctuation; **a** local wall shear stress as a function of ship speed, and **b** coefficient of friction as a function of Reynolds number; the *two curves* represent the Blasius friction law for laminar flow and the empirical coefficient of friction for turbulent flow (Schlichting 1979)

In this measurement, nominal accuracy of the shear transducer is 0.05 Pa at a frequency lower than 20 Hz (temporal response limit). The error bars in the graph indicate the standard deviation of temporally fluctuating shear stress subject to wall turbulence. It is noted that the deviation for the forward position were obtained relatively high. This occurs because the boundary layer induced from the front edge of the flat bottom intermittently keeps laminar state due to smooth wall surface. In case of bubbling, randomly distributed bubbles play a role as trigger for more stable transition to turbulent boundary layer in the beginning part of the boundary layer.

Both the wall shear stress during bubble injection (τ_{w}) and that without bubbles (τ_{w0}) were measured and time-averaged over the 7 s at $U_{\mathrm{main}} = 3.00$ m/s. From their ratio (Fig. 7), friction in the forward section intensifies with increasing α_δ except for dilute fractions $\alpha_\delta < 2.0\%$. We deduce from this trend that bubbles at high flow rates near the injector suddenly perturb the boundary layer and enhance momentum transfer, resulting in an increase in drag. In contrast, drag reduction is maintained under dilute bubble injection. At mid-ship and aft, the wall shear stress produces a well-known decline with increasing void fraction. The maximum drag reduction rate that we confirmed within the tested range is 30% at void fraction $\alpha_\delta = 4.2\%$.

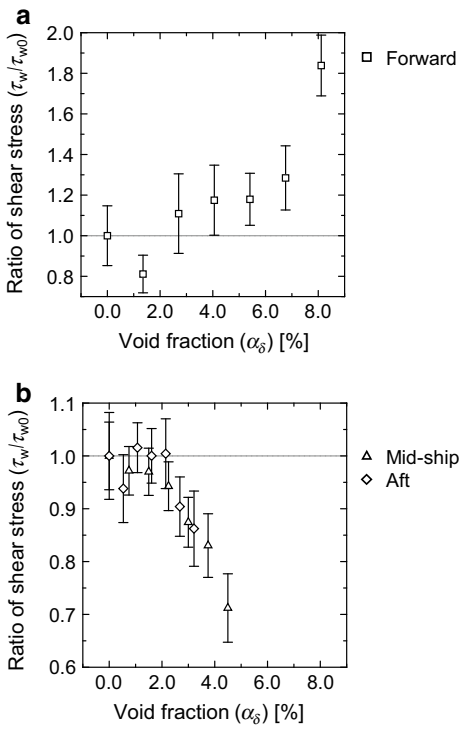

Fig. 7 Wall shear stress modified by bubble injection with respect to void fraction at a ship speed of $U_{main} = 3.00$ m/s; **a** forward, and **b** mid-ship and aft, where *error bars* indicate standard deviations

From the experimental plots, the mean impact factor of the void fraction to the drag reduction rate, defined by $(1 - \tau_w/\tau_{w0})/\alpha_\delta$ ranges from 4 to 7. An impact factor larger than unity proves that the present drag reduction is enhanced by the two-phase mutual interaction inside the boundary layer and not just because of a bulk decrease in bubble-mixed fluid density. We also found that the drag reduction curves have similar trends both at mid-ship and aft when parameterized by the boundary layer void fraction, α_δ. This suggests that drag reduction occurs with a quasi-steady mechanism between mid-ship and aft. Hence, we can analyze the behavior of bubbles within this range to elucidate the bubble-to-drag influence.

3.2 Bubble distribution

A question that has been a long-debated issue in the field of BDR research is: What kind of bubble contributes actively to drag reduction? With our fully transparent ship model, an answer does appear in a series of bubble snapshots (Fig. 8).

The snapshots are sampled from images taken with the high-speed video camera recording top views of bubbles near the wall. The camera is located mid-ship ($x \approx 2.1$ m) on the centerline close to the shear stress measurement point. From the images, the bubble sizes range widely from 1 to 50 mm. With larger U_{main}, sizes are seemingly smaller. This general trend is understandable given the bubble-shearing force, which is characterized by Weber number. For $\alpha_\delta > 2\%$, bubble size exceeds the mean bubble–bubble interval distance observed in the two-dimensionally projected top views. For $\alpha_\delta > 3\%$, bubbles occupy more than a half of the imaged area in these top views, and are likely to be an air barrier against high-speed outer flow.

To obtain the bubble size distribution, we produced a digital image from the high-speed video images. Figure 9 shows a video image of a single bubble taken under conditions $Q_g \approx 0.42 \times 10^{-3}$ m^3/s at $x \approx 3.3$ m. The bubble surface is measured by image binarization using an adequate threshold value close to the background brightness. The

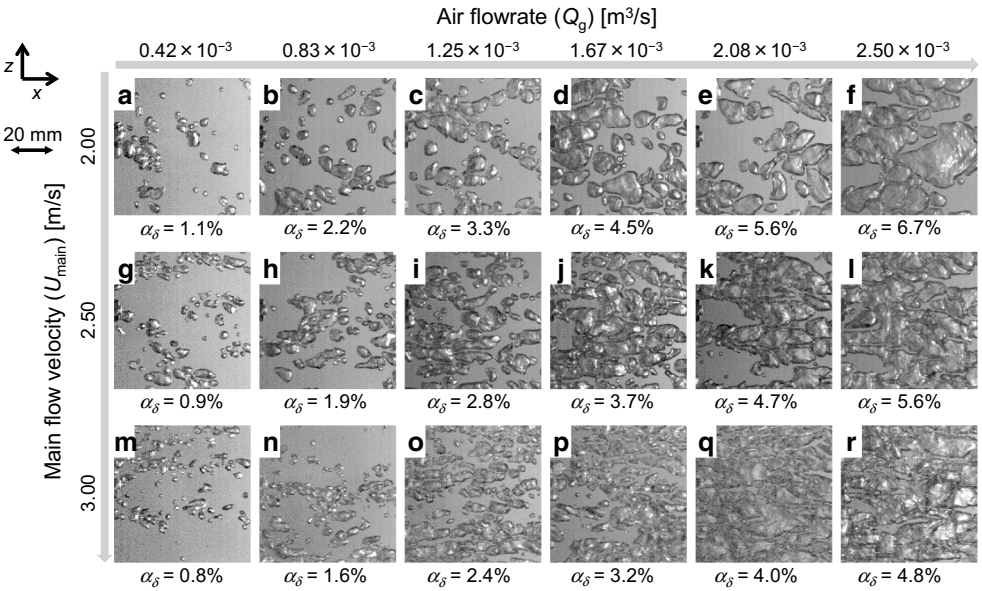

Fig. 8 Snapshots of streaming bubbles near mid-ship, $x \approx 2.1$ m; α_δ below each *panel* is the boundary layer void fraction

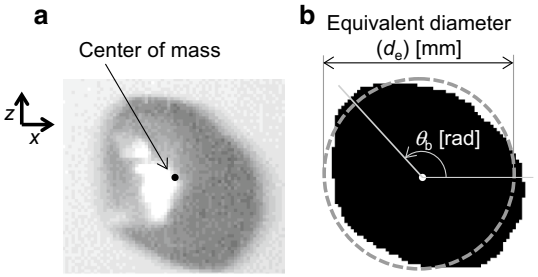

Fig. 9 Definition of equivalent diameter (d_e) and phase (θ_b) of a bubble; **a** raw image sampled from the high-speed video camera, and **b** binary image: *gray dashed line* marks the average radius of the bubble surface

coordinates of the surface are used to find the two-dimensional center of gravity of the bubble to compute the bubble velocity. The bubble size is measured from the angular average of the distance from the center to the surface coordinates; doubling the value gives the circle-equivalent bubble diameter (d_e). Figure 10 shows the probability distribution of d_e as it changes with ship speed. Note that bubbles smaller than 1 mm and larger than 8 mm are considered out of range, because the quality of back-lit imaging of their surfaces is limited.

The measured results indicate that the peak bubble diameter ranged from 3 to 4 mm as U_{main} increases from 2 to 3 m/s. This relationship is in very good agreement with the formula which Hinze (1955) proposed and Sanders et al. (2006) confirmed by experiment. Their formula describes a survivable bubble size against surrounding turbulent shear. Our present data involve both smaller and larger ones due to active fragmentation and coalescence among bubbles accumulated close to the wall. It is understandable that the theoretical survivable bubble size takes the peak population since fragmentation and coalescence rate are reversed at this criterion.

3.3 Bubble velocity

Predicting theoretically the mean bubble velocity is very difficult as the bubbles are suspended inside the turbulent boundary layer during drag reduction. Bubble velocities depend sensitively on the normal distance from wall, i.e., where the bubbles accumulate in the boundary layer in which 99% of the spread in velocity is localized.

Figure 11 shows the averaged advection velocity (u_b) of the bubbles measured by particle image velocimetry applied for bubbles imaged in Fig. 8. The error bar around each data point indicates the standard deviation from 300 sampled images. The values of u_b are roughly half of U_{mian} for all experimental conditions; this trend is basically consistent with a previous model ship study by Johansen et al. (2010). This value suggests qualitatively that the bubbly two-phase layer slides downstream creating a difference in velocity between the solid wall and the outer flow. However, an exact explanation is at present impossible to validate. From a careful look at the graphs, we find that the velocity ratio ranges between $0.45 < u_b/U_{main} < 0.65$ and rises with large U_{main} and high Q_g towing operations. Such conditions correspond to conditions for high drag reduction (see Fig. 7b). In the downstream region where the drag reduction rate relaxes, the bubble velocity ratio also relaxes. What implications does this have for a mechanism? We have found a certain relevance to void waves that we disclose in the next section.

4 Void wave measurement

During towing operations of the present model ship, we observed visually the propagation of waves constituted by the sparseness and denseness of the local bubbles on the bottom plane. In this section, we analyze the wave quantitatively. Such void waves were observed to form in spatially developing bubbly flows inside vertical pipes (Lisseter and Fowler 1992; Lammers and Biesheuvel 1996); being similar, the phenomenon we observed is termed likewise. Because these void waves can have broad spectra, we analyze the wave on two different scales as reported separately below.

4.1 Behavior of void waves

To analyze the void waves quantitatively, we used the video images taken by the underwater camera located at the stern ($x \approx 3.7$ m). Figure 12 shows instantaneous images of the bubbles beneath the bottom plane of the model ship, in which bubbles are flowing upwards. A sampling area that is marked by the thin white rectangle in the figure was chosen for a line scan of the bubbles integrated over time. Figure 13 depicts the timeline scanning image under conditions $U_{main} = 3.00$ m/s for three different Q_g values. Many lateral waves comprising bubble clusters can be seen in these timeline scanning images.

To determine the peak frequency of the void wave, the scanning images were analyzed using Fourier analysis after a background subtraction was applied. The spectra obtained are presented in Fig. 14, where the ordinate of each panel represents the bubble brightness level normalized by the maximum bubble brightness. Note that brightness is not a physical quantity, and therefore each value gives only the magnitude of the void fluctuation. The abscissa represents the frequency (f_{void}) directly obtained by frame interval time; on top is the corresponding wavelength scale, estimated using u_b/f_{void}. All the spectra are subject

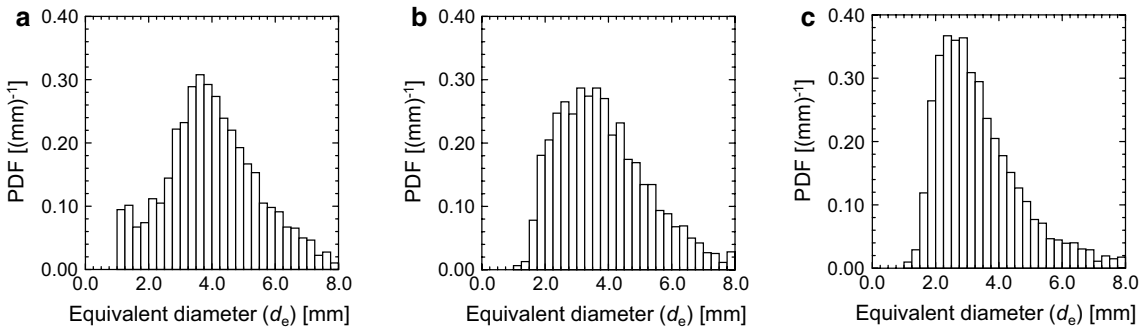

Fig. 10 Probability density distributions of the equivalent bubble diameter evaluated for $Q_g \approx 0.42 \times 10^{-3}$ m^3/s at $x \approx 3.3$ m, where small bubbles, $d_e < 1.0$ mm, are regarded as out of range; **a** $U_{main} = 2.00$ m/s, **b** 2.50 m/s and **c** 3.00 m/s

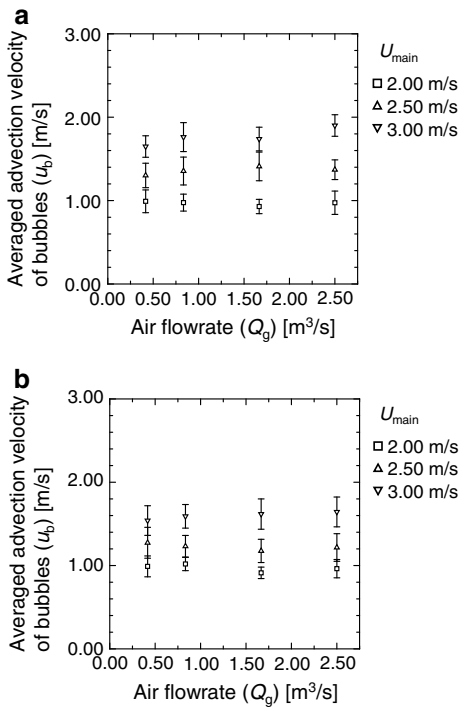

Fig. 11 Averaged advection velocity of bubbles measured at **a** $x \approx 2.1$ m and **b** 3.3 m, where *error bars* indicate standard deviations

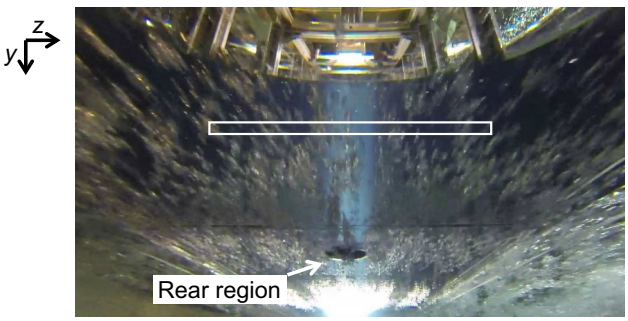

Fig. 12 Snapshot taken by the underwater camera; the framed area is located at $x \approx 3.7$ m and used to generate timeline scanning images

to broad background power because of the discrete nature of the dispersed phase. Against the background, clear peak frequencies can be seen in the range $3 < f_{void} < 8$ Hz for $Q_g = 1.67 \times 10^{-3}$ and 2.50×10^{-3} m^3/s. Within this range, there are two general trends seen in comparing the nine spectra. One is that the peak frequency rises with increasing ship speed U_{main}, particularly at high Q_G. Its rise is roughly linear with U_{main} inferring that the wavelength of the void wave is independent of ship speed. The other is that the peaks shift to lower frequencies with increasing Q_g. This trend may be attributed to the coalescence of two neighboring void waves or collapse of a single void wave in consequence of an upper limit in the local bubble number density sustainable inside a single wave. The upper limit and capacity are unclear quantitatively in this spectral analysis, and therefore we proceed to an analysis of bubble clustering.

4.2 Local bubble arrangement

To find out how the void waves are initiated and amplified at the bottom plane, we here analyze local bubble images to quantify a network-like organization of bubble distribution. Even if a peak is not observed in the void frequency spectra, many bubble clusters clearly emerge as evidenced in Figs. 13a and 14h. We believe that these mesoscale structures in the bubble distribution are perturbative source triggering the void waves. To begin, accumulations of bubbles are evaluated using distances between the centers of two bubbles (d_{cb}). The results for three different ship speeds are presented in Fig. 15, which shows probability density function (PDF) of the mutual distance. A vertical line in each panel indicates the reference distance when all the bubbles are distributed uniformly. The abscissa shows dimensional and non-dimensional scales based on the mean bubble diameter. In all three cases, the PDF has a profile weighted on the left-hand side of the reference value. For a perfectly random distribution, the reference value shifts to

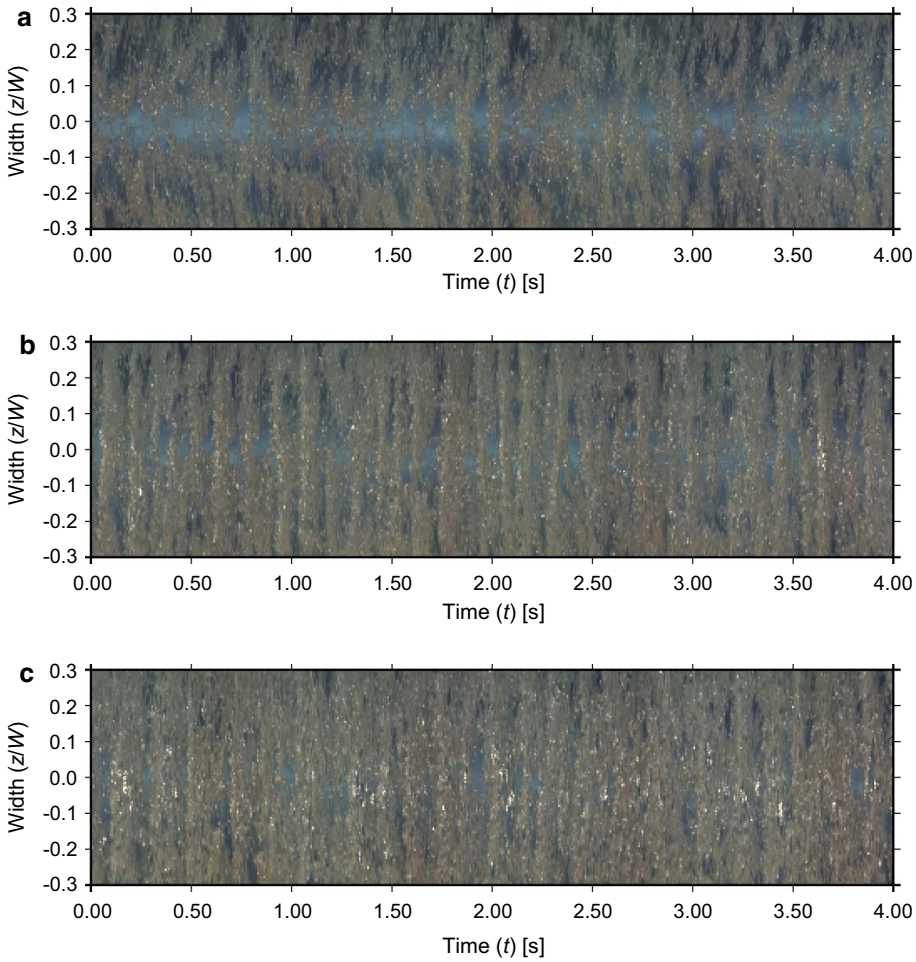

Fig. 13 Timeline scanning images taken at $x \approx 3.7$ m for $U_{main} = 3.00$ m/s; **a** $Q_g \approx 0.83 \times 10^{-3}$ m^3/s, **b** 1.67×10^{-3} m^3/s and **c** 2.50×10^{-3} m^3/s

$1/\sqrt{2}$ times the original. Nonetheless, the peak of the PDF is located to the left from the random state. This proves that bubble clusters actively form more often than that occurring naturally in a random state. Moreover, we can confirm that the peak of the PDF shifts left, i.e., toward narrower bubble spacing, as the ship speed increases. This suggests a positive correlation between drag reduction and the void wave inside which the bubble spacing narrows. In addition, it is worth noting that the spacing can be narrower than the mean bubble diameter exceeding the contact limit of spherical bubbles. This occurs mainly due to the large deviation in bubble size and may play as a role of trigger for downstream void wave generation.

We also analyzed the bubble probability distribution in the azimuthal directions. The aim of the analysis is to find a source of void wave generation from microscopic point of view. From the distribution, we subtract perfect uniform distribution in order to emphasize its anisotropy of the local bubble arrangement patterns. The result is shown in Fig. 16. The same approach was employed by Kitagawa et al. (2004) for wall-sliding bubbles along a vertical plate in a stationary liquid. They found a clear heterogeneous clustering of bubbles because of significant bubble–bubble interaction in high viscous oil. Surprisingly, the present results also show a certain statistical heterogeneity although the target is distinct from a laminar boundary layer. At $U_{main} = 2.00$ m/s, bubbles are arranged mostly in the isotropic state (see Fig. 16a). It becomes heterogeneous at $U_{main} = 2.50$ m/s and $U_{main} = 3.00$ m/s; the bubbles exhibit a high probability density at angles $\theta_b = 0$ and $\theta_b = \pi$. This implies that bubbles aggregate mainly in the streamwise direction. This is consistent with the observation (Fig. 8) that bubbles form many chains in the main direction of flow. Nierhaus et al. (2007) and Harleman et al. (2011) have reported a preferential concentration of bubbles in turbulent boundary layers, although the bubbles were smaller than coherent structures inside the boundary layer. Smith and Metzler (1983) and Zacksenhouse et al. (2001) found that the spanwise width of low-speed streaks in a single-phase turbulent boundary layer is around 100 times the friction length defined by

$$l_\tau = \frac{\nu}{\sqrt{\tau_{w0}/\rho}}. \tag{10}$$

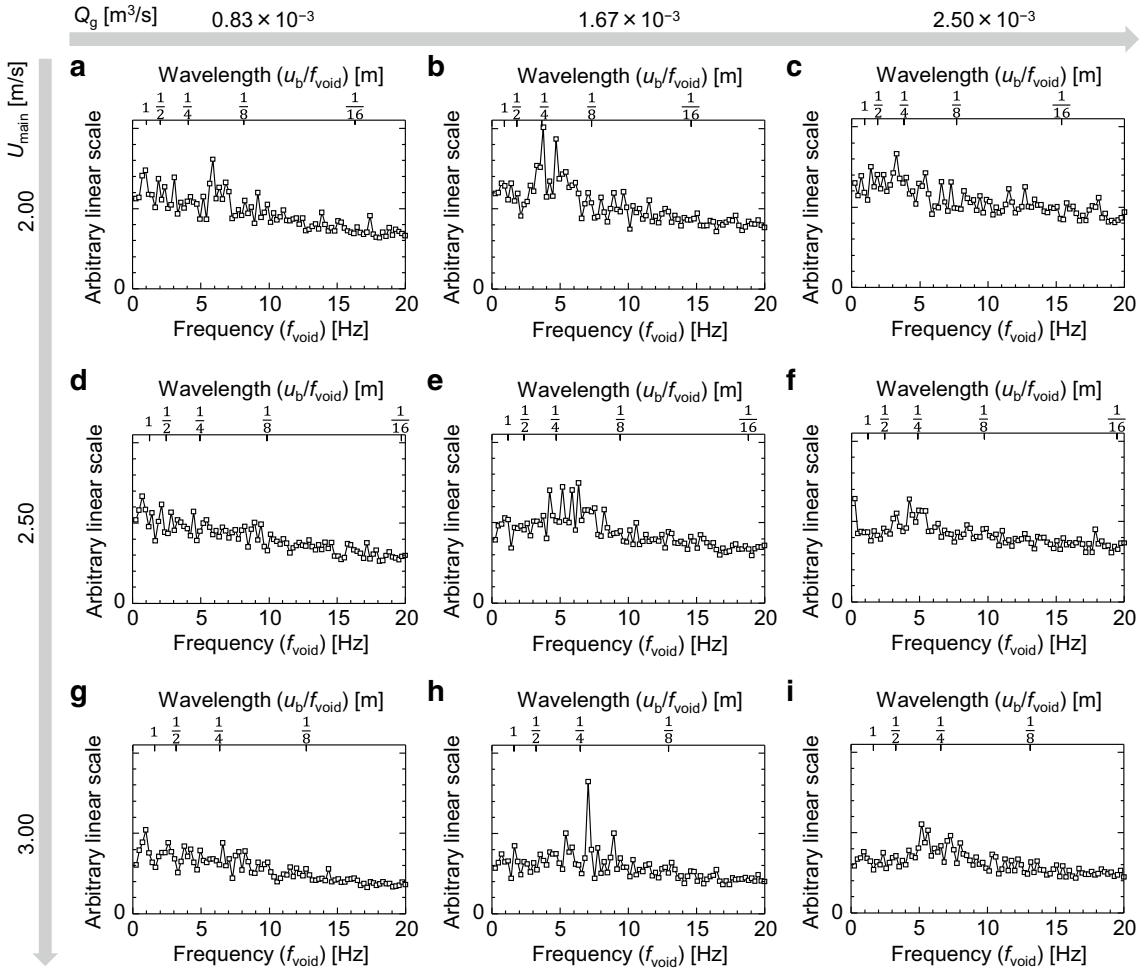

Fig. 14 Linear spectra of the void wave naturally generated underneath the flat bottom of a model ship; the spectra are obtained from timeline scanning images (e.g., Fig. 13), and given as normalized values using the maximum brightness of the images with wavelengths calculated using u_b at $x \approx 3.3$ m (see Fig. 11b)

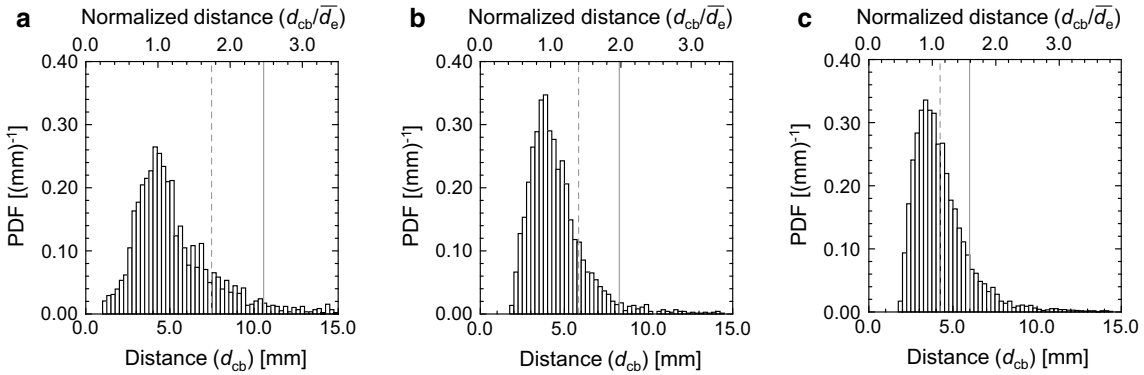

Fig. 15 Probability density distribution of the mutual distance between the closest pair of bubbles for $Q_g \approx 0.42 \times 10^{-3}$ m³/s at $x \approx 3.3$ m: **a** $U_{main} = 2.00$ m/s, **b** 2.50 m/s and **c** 3.00 m/s. Small bubbles, $d_e < 1.0$ mm, are regarded outside the analysis; the *vertical solid* and *dashed lines* indicate the distances between bubbles for perfect uniform distribution and random distribution

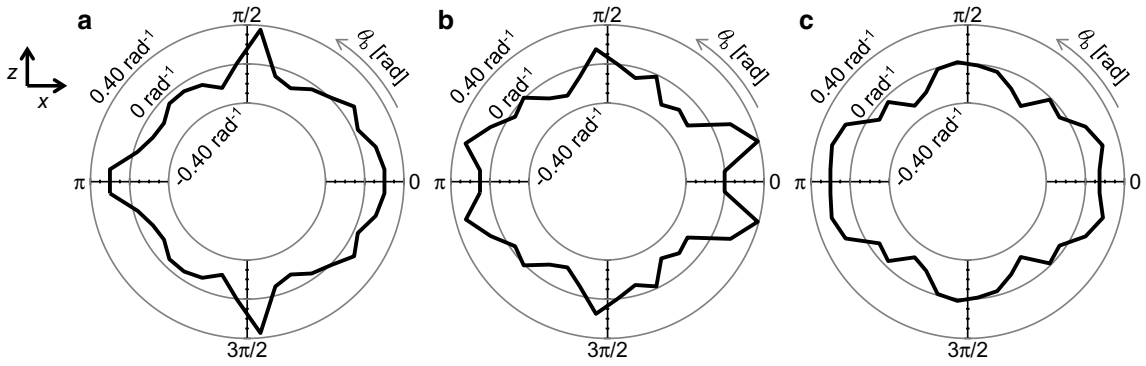

Fig. 16 Deviation of probability density distribution in the azimuthal direction of the closest bubble obtained for $Q_g \approx 0.42 \times 10^{-3}$ m^3/s at $x \approx 3.3$ m from uniform distribution: **a** $U_{main} = 2.00$ m/s, **b** 2.50 m/s, and **c** 3.00 m/s. Small bubbles, $d_e < 1.0$ mm, are regarded as outside the analysis; *gray circles* indicate values of PDF, and positive values mean higher bubble density than the uniform situation

The width has a comparable scale with that of the streamwise vortices because of coupling in a process termed a self-sustaining cycle (Hamilton et al. 1995). Therefore, 100 l_τ can be regarded as a representative length scale of the coherent structure compared with bubble size. In our experimental condition, the length scale is estimated to be approximately 0.7–1.0 mm for U_{main} in the range 2.00–3.00 m/s. Hence, the present bubble size is several times larger than the coherent structure. With such a condition, the bubble motion may be subject to a stochastic behavior that weakens the spatial structure of the bubble distribution. Nevertheless, our experimental visualization showed a clear formation of many chained bubbles. We believe a synergy arises between the local high void fraction and local drag reduction, which alters the original coherent structure inside the void wave. As this is not completely explained in the present study, we suggest this as an open problem for future research, which would be solved using artificial void waves.

5 Theoretical description of void wave

To support theoretically the wave-outstanding phenomenon in the bubbly two-phase boundary layer, we attempted to derive a wave equation for the void fraction from conservation laws. Since bubbles migrate in the horizontal direction without certain base slip velocity to liquid phase, drift flux model approach cannot be employed. Thus, the present observation of void wave is essentially different from kinematic void wave that is a wave phenomenon relying on void-to-slip correlation as reported by Pauchon and Banerjee (1988), and Lahey (1991). Even bubble's slip velocity is hardly defined since the relative velocity of the liquid phase to the bubble interface takes opposite sign between top and bottom surface of a single bubble upon high velocity gradient (e.g., Oishi and Murai (2014)). Furthermore, 100% of bubbles exist inside the turbulent boundary layer, and thereby it is important to consider the bubble motion in relevance to the wall shear stress rather in unbounded space.

5.1 Mathematical derivation

The conservation of momentum for a two-phase mixture (e.g., Murai and Matsumoto 2000) in the main direction of flow is described by

$$\rho\left(\frac{\partial fu}{\partial t}+\frac{\partial fu^2}{\partial x}+\frac{\partial fuv}{\partial y}+\frac{\partial fuw}{\partial z}\right) = -\frac{\partial p}{\partial x}+\mu\left(\frac{\partial^2 u}{\partial x^2}+\frac{\partial^2 u}{\partial y^2}+\frac{\partial^2 u}{\partial z^2}\right), \tag{11}$$

where f, p, ρ, and μ are volume fraction, pressure, density, and viscosity of liquid phase, respectively. Here f is the same as $1 - f_G$, where f_G is the local instantaneous void fraction. The velocity components, u, v, and w are those of the liquid phase in the streamwise (x), wall-perpendicular (y), and spanwise (z) directions, respectively. A spatial integration of Eq. (11) with respect to the boundary layer thickness (δ) gives

$$\int_0^\delta \frac{\partial fu}{\partial t}\mathrm{d}y+\int_0^\delta \frac{\partial fu^2}{\partial x}\mathrm{d}y+\int_0^\delta \frac{\partial fuv}{\partial y}\mathrm{d}y = -\frac{1}{\rho}\int_0^\delta \frac{\partial p}{\partial x}\mathrm{d}y+\frac{\mu}{\rho}\int_0^\delta \frac{\partial u^2}{\partial y^2}\mathrm{d}y. \tag{12}$$

Here the terms including w and z in Eq. (11) disappear through the averaging inside the boundary layer. The third term in L.H.S. of Eq. (12) is estimated as

$$\int_0^\delta \frac{\partial fuv}{\partial y}\mathrm{d}y = \left[fuv\right]_0^\delta = fuv|_\delta - fuv|_0 = fv|_\delta U_{\mathrm{main}} = VU_{\mathrm{main}}, \tag{13}$$

where U_{main} stands for flow speed outside the boundary layer. Here we assume $f = 1$ at $y = \delta$, i.e., no bubbles exist on the border of the boundary layer. V denotes the mean downward velocity of liquid phase on the border, and can be a function of time in the boundary layer flow subject to unsteadiness. However, here we treat V as constant following to the similar theory for single-phase boundary layer flows.

From volume conservation law for liquid phase, another equation stands for the same boundary layer as

$$\frac{\partial f}{\partial t} + \frac{\partial fu}{\partial x} + \frac{\partial fv}{\partial y} + \frac{\partial fw}{\partial z} = 0. \tag{14}$$

Spatial integration of Eq. (14) inside the boundary layer gives

$$\int_0^\delta \frac{\partial f}{\partial t}\mathrm{d}y + \int_0^\delta \frac{\partial fu}{\partial x}\mathrm{d}y + \int_0^\delta \frac{\partial fv}{\partial y}\mathrm{d}y = 0, \tag{15}$$

where spanwise velocity w disappears due to averaging. The third term of Eq. (15) is estimated by

$$\int_0^\delta \frac{\partial fv}{\partial y}\mathrm{d}y = \left[fv\right]_0^\delta = fv|_\delta = V. \tag{16}$$

Hence, Eq. (15) has the following relation.

$$V = -\int_0^\delta \frac{\partial f}{\partial t}\mathrm{d}y - \int_0^\delta \frac{\partial fu}{\partial x}\mathrm{d}y \tag{17}$$

Substituting Eq. (17) to Eq. (13) and then to Eq. (12), we obtain

$$\begin{aligned}\int_0^\delta \frac{\partial f(u-U_{\mathrm{main}})}{\partial t}\mathrm{d}y + \int_0^\delta \frac{\partial fu(u-U_{\mathrm{main}})}{\partial x}\mathrm{d}y \\ = -\frac{1}{\rho}\int_0^\delta \frac{\partial p}{\partial x}\mathrm{d}y + \frac{\mu}{\rho}\int_0^\delta \frac{\partial u^2}{\partial y^2}\mathrm{d}y.\end{aligned} \tag{18}$$

Hereafter, we use boundary-layer-averaged quantities, which are defined by

$$\alpha_\delta = \frac{1}{\delta}\int_0^\delta (1-f)\mathrm{d}y, \quad U_\delta = \frac{1}{\delta}\int_0^\delta u\mathrm{d}y. \tag{19}$$

Each term in Eq. (18) is therefore linearly approximated as

$$\int_0^\delta \frac{\partial f(u-U_{\mathrm{main}})}{\partial t}\mathrm{d}y = \delta\left\{\frac{\partial(1-\alpha_\delta)(U_\delta - U_{\mathrm{main}})}{\partial t}\right\}, \tag{20}$$

$$\int_0^\delta \frac{\partial fu(u-U_{\mathrm{main}})}{\partial x}\mathrm{d}y = \delta\left\{\frac{(1-\alpha_\delta)U_\delta(U_\delta - U_{\mathrm{main}})}{\partial x}\right\}, \tag{21}$$

and

$$\begin{aligned}-\frac{1}{\rho}\int_0^\delta \frac{\partial p}{\partial x}\mathrm{d}y + \frac{\mu}{\rho}\int_0^\delta \frac{\partial u^2}{\partial y^2}\mathrm{d}y &= 0 + \frac{\mu}{\rho}\left[\frac{\partial u}{\partial y}\right]_0^\delta \\ &= \frac{\mu}{\rho}\left(0 - \left.\frac{\partial u}{\partial y}\right|_\delta\right) = -\frac{\tau_{\mathrm{w}}}{\rho}.\end{aligned} \tag{22}$$

Equation (15) satisfying Eq. (16) can be also rewritten as

$$\frac{\partial(1-\alpha_\delta)}{\partial t} + \frac{\partial(1-\alpha_\delta)U_\delta}{\partial x} = -V. \tag{23}$$

Using Eqs. (20)–(23), Eq. (18) can be simplified as

$$\frac{\partial(1-\alpha_\delta)U_\delta}{\partial t} + \frac{\partial(1-\alpha_\delta)U_\delta^2}{\partial x} = -\frac{\tau_{\mathrm{w}}}{\rho\delta} + VU_{\mathrm{main}}. \tag{24}$$

The derivation of Eq. (24) from Eq. (11) is in part similar to von Karman's momentum integral approach for a single-phase spatially developing boundary layer. In our case, void fraction profile as functions of time and streamwise coordinate, $\alpha_\delta(x, t)$, is taken into account under the condition of $\alpha_\delta = 0$ at $y = \delta$.

Equation (23) also produces following equation as being taking derivative in time,

$$\frac{\partial^2(1-\alpha_\delta)}{\partial t^2} + \frac{\partial}{\partial x}\left(\frac{\partial(1-\alpha_\delta)U_\delta}{\partial t}\right) = 0. \tag{25}$$

As the first term of Eq. (24) is identical to the time differential in the second term above, Eq. (25) is rewritten as

$$\frac{\partial^2\alpha_\delta}{\partial t^2} + \frac{\partial}{\partial x}\left(\frac{\partial(1-\alpha_\delta)U_\delta^2}{\partial x} + \frac{\tau_{\mathrm{w}}}{\rho\delta}\right) = 0. \tag{26}$$

This equation expands to give

$$\frac{\partial^2\alpha_\delta}{\partial t^2} + (1-\alpha_\delta)\frac{\partial^2 U_\delta^2}{\partial x^2} = U_\delta^2\frac{\partial^2\alpha_\delta}{\partial x^2} - \frac{\partial}{\partial x}\left(\frac{\tau_{\mathrm{w}}}{\rho\delta}\right). \tag{27}$$

In a slowly developing boundary layer, the second term on the left-hand side in Eq. (27) is negligible compared with other terms, and thus we obtain

$$\frac{\partial^2 \alpha_\delta}{\partial t^2} = U_\delta^2 \frac{\partial^2 \alpha_\delta}{\partial x^2} - \frac{\partial}{\partial x}\left(\frac{\tau_w}{\rho \delta}\right). \tag{28}$$

Noe that τ_w in Eqs. from (22) to (28) stands for the shear stress acting on fluid at the wall, but not on the wall. In order to avoid confusion due to action–reaction force law, let us rewrite Eq. (28) reversing the sign as

$$\frac{\partial^2 \alpha_\delta}{\partial t^2} = U_\delta^2 \frac{\partial^2 \alpha_\delta}{\partial x^2} + \frac{\partial}{\partial x}\left(\frac{\tau_w}{\rho \delta}\right), \tag{29}$$

Now this equation expresses the relationship among local void fraction, local flow speed, and local wall shear stress that acts on the wall.

5.2 Void wave equation

Our problem is how to model the wall shear stress in Eq. (29). Let us assume a wall shear stress given as an experimentally correlated model,

$$\tau_w = \tau_{w0}\left(1 - G_1 \alpha_\delta - G_2 \frac{\partial \alpha_\delta}{\partial x}\right), \tag{30}$$

where τ_{w0} denotes wall shear stress in the absence of bubbles, i.e., the original value before bubble injection. The parameter G_1 represents an impact factor for drag reduction to void fraction supplied inside the boundary layer. The performance of G_1 for a variety of flow conditions was previously reported by Murai (2014). The other parameter G_2 in Eq. (30) is a new term that describes the impact of the local gradient of the void fraction. This term is modeled based on a previous finding that local wall shear stress has a significant phase shift in the oscillatory fluctuation of the local void fraction (Oishi et al. 2009). The two parameters, G_1 and G_2, can take both positive and negative values depending on bubble size and flow speed. We emphasize that there is no physical evidence why these two terms are linearly additive to describe local wall shear stress. That is, Eq. (30) simply expresses a mathematical constitution of the wall shear stress composed of the first two derivative terms with respect to void fraction, i.e., $\alpha_\delta^{(0)}$ and $\alpha_\delta^{(1)}$. Beside it, the authors are not insisting that the term with G_1 would be replaced with the term with G_2 in interpretation of bubble drag reduction since both terms stand simultaneously and contribute to independent phenomena.

Substituting Eq. (30) into Eq. (29) obtains

$$\frac{\partial^2 \alpha_\delta}{\partial t^2} = U_\delta^2 \frac{\partial^2 \alpha_\delta}{\partial x^2} + \frac{\tau_{w0}}{\rho \delta}\left(-G_1 \frac{\partial \alpha_\delta}{\partial x} - G_2 \frac{\partial^2 \alpha_\delta}{\partial x^2}\right), \tag{31}$$

which is rearranged to give

$$\frac{\partial^2 \alpha_\delta}{\partial t^2} = C^2 \frac{\partial^2 \alpha_\delta}{\partial x^2} - G_1 \frac{\tau_{w0}}{\rho \delta} \frac{\partial \alpha_\delta}{\partial x}, \quad C^2 = U_\delta^2 - G_2 \frac{\tau_{w0}}{\rho \delta}. \tag{32}$$

Equation (32) takes the form of a wave equation for void fraction. Hence, it supports mathematically that the generation of the void wave is inherent to the system that accompanies drag reduction. Equation (32) also indicates that the void fraction propagates with speed (C) that decreases with G_2. This is consistent with the present experimental observation, i.e., void waves propagate at a speed significantly slower than the ship speed. The value of G_2 is estimated from the present experimental result to be approximately

$$G_2 = \frac{2\delta}{C_f}\left[1 - \left(\frac{C}{U_\delta}\right)^2\right] \approx \frac{0.1\,\mathrm{m}}{0.003}\left[1 - (0.6)^2\right] \approx 21\,\mathrm{m}. \tag{33}$$

Here 99% thickness of boundary layer is adopted for δ for which U_δ is estimated by $(7/8)U_{main}$. The estimated value of G_2 means that bubbles have a transient effect on drag reduction within 21 m in the main direction of flow, being much longer than the boundary layer thickness. It also infers that the wavelength of the void wave is shorter than 21 m. From another perspective, void waves do not amplify themselves for wavelengths longer than 21 m in the range tested because transients no longer are present beyond this length. The second term in Eq. (32) plays the role of a source term in the wave equation. When the value of G_1 is high, the wave is initiated.

Note that the present attempt at a theoretical description only proves the potential existence of void waves in the system, but does not provide a mechanism for generation or a determination of its wavelength. We are presently studying this phenomenon using artificially generated void waves in the upstream location to observe its amplification along the main direction of flow. We shall report on this aspect in a separate contribution.

6 Conclusions

We designed a 4-m-long model ship with a fully transparent flat bottom plate to investigate frictional drag reduction following the injection of air bubbles. Various measurement instruments were incorporated into the model ship, including a high-speed video camera for imaging bubbles from above, an underwater camera to capture the behavior of bubbles, ultrasonic measurement systems, and wall friction measurement systems. The model ship was towed in a 100-m-long water reservoir, to confirm drag reduction of up to 30% at an average void fraction of 5% inside the

turbulent boundary layer. In this paper, details of the ship design and measurement systems were presented, particularly regarding void waves generated entirely along the ship bottom. Through image processing of several sets of bubble behavior visualizations, we confirmed that the average bubble streaming velocity is approximately half the ship's speed. We observed clearly formed void waves having a distinct wavelength irrespective of ship speed under the conditions tested. The void waves involve local heterogeneous bubble clustering, which was confirmed statistically in a pattern analysis of bubble arrangement. Because void waves stand out when drag reduction becomes effective, we attempted mathematically to derive a wave equation for void fraction. The wave equation originates from a contributing term to drag reduction that depends on the spatial gradient of void fraction. This term also constrains the propagating speed of the void fraction wave relative to the ship speed.

Throughout this experiment, our detailed measurements of bubble behavior have suggested spin-off questions regarding bubbly two-phase turbulent boundary layer dynamics during drag reduction. We leave these issues as open problems from which we expect further advances in scientific understanding as well as practical improvements in ship drag reduction.

Acknowledgements This work was supported by the Fundamental Research Developing Association for Shipbuilding and Offshore (REDAS), Grant-in-Aid for JSPS Fellows No. 15J00147, JSPS KAKENHI Grant Nos. 24246033 and 23760143, and Grant-in-Aid for Young Scientists (B) No. 16K18006. The authors express their appreciation for all the support. Also, the authors express thanks to Prof. Yasukawa of Hiroshima University for his full support during the towing experiments at the Graduate School of Engineering.

References

Amromin E, Karafiath G, Metcalf B (2011) Ship drag reduction by air bottom ventilated cavitation in calm water and in waves. J Ship Res 55:196–207

Ceccio SL (2010) Frictional drag reduction of external flow with bubble and gas injection. Annu Rev Fluid Mech 42:183–203

Foeth EJ, Eggers R, Quadvlieg EHHA (2010) The efficiency of air-bubble lubrication for decreasing friction resistance, Paper no. 12. Prof Int Conf Ship Drag Reduction (SMOOTH-SHIP), Istanbul, Turkey

Fukuda K, Tokunaga J, Nobunaga T, Nakatani T, Iwasaki T (2000) Frictional drag reduction with air lubricant over a super-water-repellent surface. J Mar Sci Technol 5:123–130

Hamilton JM, Kim J, Waleffe F (1995) Regeneration mechanisms of near-wall turbulence structures. J Fluid Mech 287:317–348

Harleman MJW, Delfos R, Terwisga TJCV, Westerweel J (2011) Dispersion of bubbles in fully developed channel flow. J Phys Conf Ser 318:052007

Hinze JO (1955) Fundamentals of the hydrodynamic mechanism of splitting in dispersion processes. AIChE J 1:289–295

Hirayama A, Soejima S, Miyata H, Tatsui T, Kasahara Y, Okamoto Y, Iwasaki Y, Shimoyama N (2003) A study of air lubrication method to reduce frictional resistance of ship—an experimental study using flat plate and 16 m-model. In: West-Japan Society of Naval Architects meeting, vol 105, pp 1–9 **(in Japanese)**

Jang J, Choi SH, Ahn S, Kim B, Seo JS (2014) Experimental investigation of frictional resistance reduction with air layer on the hull bottom of a ship. Int J Nav Archit Ocean Eng 6:363–379

Johansen J, Castro AM, Carrica P (2010) Full-scale two-phase flow measurements on Athena research vessel. Int J Multiphase Flow 36:720–737

Katsui T, Okamoto Y, Kasahara Y, Shimoyama N, Iwasaki Y, Soejima S (2003) A study of air lubrication method to reduce frictional resistance of ship: experimental investigation by tanker form model ship and estimation of full scale ship performance. J Kansai Soc Nav Archit Jpn 239:45–53 **(in Japanese)**

Kitagawa A, Sugiyama K, Murai Y (2004) Experimental detection of bubble–bubble interactions in a wall-sliding bubble swarm. Int J Multiphase Flow 30:1213–1234

Kodama Y, Kakugawa A, Takahashi T, Kawashima H (2000) Experimental study on microbubbles and their applicability to ships for skin friction reduction. Int J Heat Fluid Flow 21:582–588

Kumagai I, Takahashi Y, Murai Y (2015) A new power-saving device for air bubble generation using a hydrofoil for reducing ship drag: theory, experiments, and applications to ships. Ocean Eng 95:183–194

Lahey RT Jr (1991) Void wave propagation phenomena in two-phase flow. AIChE J 37:123–135

Lammers JH, Biesheuvel A (1996) Concentration waves and the instability of bubbly flows. J Fluid Mech 328:67–93

Latorre R, Miller A, Philips R (2003) Micro-bubble resistance reduction on a model SES catamaran. Ocean Eng 30:2297–2309

Lisseter PE, Fowler AC (1992) Bubbly flow—II: Modelling void fraction waves. Int J Multiphase Flow 18:205–215

Madavan NK, Deutsch S, Merkle CL (1984) Reduction of turbulent skin friction by microbubbles. Phys Fluids 27:356–363

Mäkiharju SA, Elbing BR, Wiggins A, Schinasi S, Vanden-Broeck JM, Perlin M, Dowling DR, Ceccio SL (2013) On the scaling of air entrainment from a ventilated partial cavity. J Fluid Mech 732:47–76

McCormick M, Bhattacharyya R (1973) Drag reduction of a submersible hull by electrolysis. Nav Eng J 85:11–16

Mercado JM, Gómez DC, van Gils D, Sun C, Lohse D (2010) On bubble clustering and energy spectra in pseudo-turbulence. J Fluid Mech 650:287–306

Mizokami S, Kawakado M, Kawano M, Hasegawa T, Hirakawa I (2013) Implementation of ship energy-saving operations with Mitsubishi air lubrication system. MHI Tech Rev 50:44–49

Mori K, Imanishi H, Tsuji Y, Hattori T, Matsubara M, Mochizuki S (2009) Direct total skin-friction measurement of a flat plate in zero-pressure-gradient boundary layers. Fluid Dyn Res 41:021406

Murai Y (2014) Frictional drag reduction by bubble injection. Exp Fluids 55:1733

Murai Y, Matsumoto Y (2000) Numerical study of the three-dimensional structure of a bubble plume. J Fluids Eng 122:754–760

Murai Y, Fukuda H, Oishi Y, Kodama Y, Yamamoto F (2007) Skin friction reduction by large air bubbles in a horizontal channel flow. Int J Multiphase Flow 33:147–163

Nierhaus T, Vanden Abeele D, Deconinck H (2007) Direct numerical simulation of bubbly flow in the turbulent boundary layer of a horizontal parallel plate electrochemical reactor. Int J Heat Fluid Flow 28:542–551

Oishi Y, Murai Y (2014) Horizontal turbulent channel flow interacted by a single large bubble. Exp Thermal Fluid Sci 55:128–139

Oishi Y, Murai Y, Tasaka Y, Takeda Y (2009) Frictional drag reduction by wavy advection of deformation bubbles. J Phys Conf Ser 147:012020

Park HJ, Tasaka Y, Oishi Y, Murai Y (2015a) Drag reduction promoted by repetitive bubble injection in turbulent channel flows. Int J Multiphase Flow 75:12–25

Park HJ, Tasaka Y, Murai Y (2015b) Ultrasonic pulse echography for bubbles traveling in the proximity of a wall. Meas Sci Technol 26:125301

Pauchon C, Banerjee S (1988) Interphase momentum interaction effects in the averaged multifield model. Part II: Kinematic wave and interfacial drag in bubbly flows. Int J Multiphase Flow 14:253–264

Sanders WC, Winkel ES, Dowling DR, Perlin M, Ceccio SL (2006) Bubble friction drag reduction in a high-Reynolds-number flat-plate turbulent boundary layer. J Fluid Mech 552:353–380

Schlichting H (1979) Boundary-layer theory, 7th edn. McGraw-Hill Higher Education, New York

Smith CR, Metzler SP (1983) The characteristics of low-speed streaks in the near-wall region of a turbulent boundary layer. J Fluid Mech 129:27–54

Takagi S, Matsumoto Y (2011) Surfactant effects on bubble motion and bubbly flows. Annu Rev Fluid Mech 43:615–636

Takahashi T, Kakugawa A, Makino M, Kodama Y (2003) Experimental study on scale effect of drag reduction by microbubbles using very large flat plate ships. J Kansai Soc Nav Archit Jpn 239:11–20 **(in Japanese)**

Takeuchi T, Kagawa T (2013) Applicability of frequency response test for stability evaluation of gas pressure regulator. Trans Soc Instrum Control Eng 49:747–754 **(in Japanese)**

Titov I (ed) (1975) Practical problems in ship hydromechanics. Sudostroeniye Publishing Hose, Leningrad (in Russian)

Tokunaga K (1987) Reduction of frictional resistance of a flat plate by microbubbles. In: West-Japan Society of Naval Architects meeting, vol 73, pp 79–82

Watanabe O, Masuko A, Shirose Y (1998) Measurements of drag reduction by microbubbles using very long ship models. J Soc Nav Archit Jpn 1998:53–63

Yim KT, Kim H (1996) On the variation of resistance components due to air bubble blowing on bulb surface of a ship. Trans SNAK 33:54–64 **(in Korean)**

Zacksenhouse M, Abramovich G, Hetsroni G (2001) Automatic spatial characterization of low-speed streaks from thermal images. Exp Fluids 31:229–239